Electronic-state-resolved analysis of high-enthalpy air plasma flows

Sung Min Jo[*] and Oh Joon Kwon[†]
Korea Advanced Institute of Science and Technology, Daejeon 34141, Republic of Korea

Jae Gang Kim[‡]
Sejong University, Seoul 05006, Republic of Korea

(Received 20 May 2019; published 5 September 2019)

In the present study, three different electronic state-to-state methods are proposed to analyze nonequilibrium air plasma flows behind a strong shock wave. In the first approach representing the conventional method, a two-temperature model combined with the electronic quasi-steady-state assumption is adopted. In the second and the third methods, atomic and molecular electronic master equations are coupled with a conservation equation to describe the electronic state-to-state kinetics. State-of-the-art electronic transition rates for atmospheric gas species are compiled with comparisons of existing data. A prediction of the measured nonequilibrium radiation is made for the flow conditions of recent electric-arc shock tube experiments. In a comparison with the measured spectrum, the present electronic master equation coupling methods are more accurate than the conventional approach when used to estimate the initial rising rate and peak value of the diatomic intensity and small amounts of atomic radiation when the diatomic nonequilibrium condition is dominant. Moreover, the spatial distributions of the intensity and electron number density are more accurately predicted by the present methods when the flow fields are dominated by atomic nonequilibrium.

DOI: 10.1103/PhysRevE.100.033203

I. INTRODUCTION

Behind a strong shock wave, various physicochemical processes simultaneously occur. In the relaxation period, high-temperature gas in a thermochemical nonequilibrium state is electronically excited and ionized by collisional processes. High-lying electronic levels emit radiative energy that can heat the surfaces of a hypersonic vehicle. In this case, an accurate prediction of such nonequilibrium relaxation phenomena is one of the most important factors when designing a thermal protection system. Physical validity of nonequilibrium models can be assessed by predicting the measured data obtained from flight and ground tests. A flight test provides the most accurate data related to the heat flux on the surface [1]. However, substantial expenses are required for flight tests, and the process of the collisional-radiative (CR) transitions occurring immediately behind a shock wave cannot be measured in detail during the flight test. For these reasons, several ground tests have been conducted to study the relaxation processes.

Recently, nonequilibrium air radiation has been newly measured in the NASA Ames Electric-Arc Shock Tube (EAST) facility for various earth reentry flow conditions [2–5]. In these studies, quantitative parametrization of artificial smearing functions, such as the instrumental line shape (ILS) and the spatial resolution function (SRF), was also performed. The resultant parameters [6] of ILS and SRF are available to the hypersonic community. This enables researchers to reproduce the measured spectra in the spatial and spectral domains to validate the accuracy of their nonequilibrium models.

Together with ground tests, numerical studies in predicting measured nonequilibrium radiation have been conducted by several research groups [3,7–10]. In previous studies [3,7–9], simulations were performed based on the conventional two-temperature (2T) model [1] with the electronic quasi-steady-state (QSS) assumption [1]. In the numerical modeling by Panesi *et al.* [10], the electronic QSS assumption was eliminated by coupling a set of electronic master equations (EMs) for atomic species to one-dimensional Euler equations. However, a comparison with measured radiation was only done for spectral ranges above 700 nm. A large amount of modeling uncertainty still exists in the vacuum ultraviolet (VUV) and UV wavelength ranges [3]. Therefore, further investigations of CR transitions based on a non-QSS approach and a more accurate thermochemical nonequilibrium model should be performed for different and wider wavelength ranges.

Toward this end, in the present study, three-different physical models are proposed to analyze nonequilibrium air plasma flows behind a strong shock wave. In the first approach, the conventional 2T model is utilized together with the electronic QSS assumption to calculate the flow field and electronic state populations. In the second and the third approaches, the processes of CR transitions in a flow field are modeled in more detail. For this purpose, EM coupled models are devised by separating the species electronic energy and the free electron translational energy from the conventional 2T model. In the EM coupled models, the atomic master equation and the atomic and molecular master equation are separately

[*]smjo@kaist.ac.kr
[†]Corresponding author: ojkwon@kaist.ac.kr
[‡]Corresponding author: jaegkim@sejong.ac.kr

TABLE I. Species electronic levels considered in the electronic master equation.

Species	State	Source
N	1–27: ungrouped, 28–38: grouped for same n_p	[1,11,12]
O	1–27: ungrouped, 28–32: grouped for same n_p	[1,12]
N_2	1–5 ($X^1\Sigma_g^+$, $A^3\Sigma_u^+$, $B^3\Pi_g$, $W^3\Delta_u$, $B'^3\Sigma_u^-$)	[13–16]
N_2^+	1–4 ($X^2\Sigma_g^+$, $A^2\Pi_u$, $B^2\Sigma_u^+$, $D^2\Pi_g$)	[13–16]
O_2	1–4 ($X^3\Sigma_g^-$, $a^1\Delta_g$, $b^1\Sigma_g^+$, $c^1\Sigma_u^-$)	[13,16]
NO	1–5 ($X^2\Pi$, $a^4\Pi$, $A^2\Sigma^+$, $B^2\Pi$, $b^4\Sigma^-$)	[13,14,16]

considered to evaluate the non-Boltzmann distribution effect of the atomic and molecular electronic populations, with these denoted as the EM-atom and EM-air models, respectively. The electronic master equations in the EM coupled models are tightly coupled with one-dimensional conservation equations to eliminate the electronic QSS assumption. In the present study, an assessment including both electron and heavy-particle impacts is carried out to construct the best available database of electronic state-to-state rates. The nonequilibrium radiation prediction is then made in the wavelength range from VUV to infrared (IR) for the flow conditions of an EAST measurement using the 2T-QSS and EM coupled models of EM-atom and EM-air. In comparisons with measured data, nonequilibrium phenomena are investigated in detail. The influence of the QSS assumption on the flow field calculation is studied by comparing the distributions of the electronic state population. Moreover, vulnerable aspects of the conventional 2T model combined with the QSS assumption in predictions of nonequilibrium radiation are discussed in detail.

II. COLLISIONAL-RADIATIVE MODELING OF AIR PLASMA FLOWS

In the present study, three different methods, denoted as 2T-QSS, EM-atom, and EM-air, are devised to model the electronic state-to-state processes occurring in a postshock region. In total, 11 global species, N, N_2, N_2^+, O, O_2, NO, N^+, O^+, O_2^+, NO^+, and e^-, are considered to describe the flow field. For the N, N_2, N_2^+, O, O_2, and NO species, the electronic master equations are calculated to evaluate the distributions of the electronic state population. In Table I, the species electronic states used when analyzing the electronic master equation are summarized. In neutral atoms, the electronic levels in high-energy states are grouped using the principal quantum number, n_p. Individual multiplets of grouped atomic states are assumed to follow Boltzmann distributions. Details of the electronic levels for N and O, in this case the term energy, degeneracy, and principal quantum number, are presented in Table II. The dissociation limit is applied to calculate the electronic populations of the diatomic states, which are not included in the master equation analyses but are considered in the radiation calculations. In the ionized species of N^+, O^+, O_2^+, and NO^+, where the electronic master equations are difficult to apply, it is assumed that the electronic distribution has a Boltzmann distribution specified with the electronic temperature. In N^+ and O^+, 15 electronic grouping levels are utilized. In O_2^+ and NO^+, four and eight electronic states are utilized, respectively. The required spectroscopic constants are obtained from various sources [1,11–16].

For the calculation of the flow properties, a postshock flow solver including the effects of thermochemical nonequilibrium is developed. The Rankine-Hugoniot relations assuming the vibrational and electronic energy modes to be frozen are utilized to evaluate postshock conditions immediately behind a strong shock wave. Subsequently, one-dimensional conservation equations of mass, momentum, and global energy are solved to calculate the downstream flows. These equations can be written as

$$\frac{\partial}{\partial x}\begin{bmatrix}\rho_s u\\ \rho u^2+p\\ \rho u(h+u^2/2)\end{bmatrix}=\begin{bmatrix}m_s\omega_s\\ 0\\ -Q_{\rm rad}\end{bmatrix}, \tag{1}$$

where ρ, u, and m are the density, velocity, and the mass, respectively, and s is the species index. In addition, p, h, and ω are the pressure, specific enthalpy, and the rate of formation of the species number density. The energy loss due to radiative transition, $Q_{\rm rad}$, is set to zero in the 2T-QSS method, whereas in the EM coupled models of EM-atom and EM-air, it is modeled by considering the bound-bound transitions and the radiative and dielectronic recombination processes. In addition to Eq. (1), the electron-electronic-vibrational energy equation of the 2T model and the electronic master equations of the EM coupled models are calculated to analyze the postshock flows.

A. Two-temperature model with the quasi-steady-state assumption

In the conventional 2T model [1], the thermal modes are decomposed into two parts: the translational-rotational and the electron-electronic-vibrational energy modes. These are denoted as the transrotational temperature $T_{\rm tr}$ and the electron-electronic-vibrational temperature $T_{\rm eev}$, respectively. The electron-electronic-vibrational energy conservation equation is then determined using the expression

$$u\frac{\partial E_{\rm eev}}{\partial x}=\Omega_{v\text{-}T}+\Omega_{e\text{-}T}+\Omega_{c\text{-}v}+\Omega_{c\text{-}e}, \tag{2}$$

where $E_{\rm eev}$ is the electron-electronic-vibrational energy. The vibrational-translational energy transfer rate, $\Omega_{v\text{-}T}$, is assumed to follow a Landau-Teller formula,

$$\Omega_{v\text{-}T}=\sum_s^m\frac{E_{{\rm vib},s}(T_{\rm tr})-E_{{\rm vib},s}(T_{\rm eev})}{\tau_{v\text{-}c,s}}, \tag{3}$$

where m is the group of molecules and $\tau_{v\text{-}c,s}$ is the Millikan-White relaxation time [17] including collision-limited correction for high-temperature conditions [1,18,19]. The species vibrational energy is denoted as $E_{{\rm vib},s}$. The electron-translational energy (ET) exchange rate, $\Omega_{e\text{-}T}$, is modeled by the rate equation derived by Appleton and Bray [20]:

$$\Omega_{e\text{-}T}=\sum_s^H 3\gamma_e m_e N_a k(T_{\rm tr}-T_{\rm eev})\frac{\nu_{e,s}}{m_s}. \tag{4}$$

In this equation, H and γ_e are correspondingly the group of the heavy particles and the concentration of electrons. Additionally, N_a and k represent Avogadro's number and the

TABLE II. Details of the electronic levels of N and O.

State for N	Energy, cm^{-1}	Degeneracy	n_p	State for O	Energy, cm^{-1}	Degeneracy	n_p
1	0	4	2	1	78	9	2
2	19 228	10	2	2	15 868	5	2
3	28 839	6	2	3	33 792	1	2
4	83 336	12	3	4	73 768	5	3
5	86 193	6	3	5	76 795	3	3
6	88 132	12	2	6	86 629	15	3
7	93 582	2	3	7	88 631	9	3
8	94 838	20	3	8	95 477	5	4
9	95 510	12	3	9	96 226	3	4
10	96 751	4	3	10	97 421	25	3
11	96 833	10	3	11	97 489	15	3
12	97 794	6	3	12	99 095	15	4
13	99 664	10	3	13	99 682	9	4
14	103 694	12	4	14	101 144	15	3
15	104 196	6	4	15	102 117	5	5
16	104 628	6	3	16	102 413	3	5
17	104 720	28	3	17	102 663	5	3
18	104 849	14	3	18	102 866	25	4
19	104 852	12	3	19	102 909	15	4
20	105 007	20	3	20	102 968.3	35	4
21	105 134	10	3	21	102 968.4	21	4
22	106 478	2	4	22	103 627	15	5
23	106 823	20	4	23	103 871	9	5
24	107 014	12	4	24	105 386	25	5
25	107 225	10	4	25	105 410	15	5
26	107 446	4	4	26	105 441.6	35	5
27	107 615	6	4	27	105 441.7	21	5
28	110 021	18	5	28	106 634	288	6
29	110 315	90	4	29	107 578	392	7
30	110 486	126	4	30	108 112	512	8
31	111 363	54	5	31	108 473	648	9
32	112 851	90	5	32	108 729	800	10
33	112 929	288	5	–	–	–	–
34	114 298	648	6	–	–	–	–
35	115 107	882	7	–	–	–	–
36	115 631	1152	8	–	–	–	–
37	115 991	1458	9	–	–	–	–
38	116 248	1800	10	–	–	–	–

Boltzmann constant, respectively. The collision frequency, $\nu_{e,s}$ is calculated as

$$\nu_{e,s} = n_s \sigma_{e,s} \left(\frac{8kT_{\text{eev}}}{\pi m_e} \right)^{1/2}, \tag{5}$$

where $\sigma_{e,s}$ is the effective collision cross section. For the collisions between electrons and neutral species, the effective collision cross section is determined using the curve fit of Gnoffo *et al.* [21]. For the collisions between electrons and the ionized species, the Debye cutoff approximation [1] is applied to calculate the cross section.

The rate of chemistry-vibrational energy coupling, $\Omega_{c\text{-}v}$, is evaluated by applying a preferential dissociation model,

$$\Omega_{c\text{-}v} = \sum_{r}^{R_i} \sum_{i}^{m} \psi_i \omega_{r,i} D_{r,i} N_a, \tag{6}$$

where R_i and $D_{r,i}$ are the group of reactions and the reaction enthalpy related to net production of the ith molecule, respectively. The vibrational energy loss ratio, ψ_i, is obtained from the results of the master equation calculations [18,19]. The rate of chemistry-electron-electronic energy coupling, $\Omega_{c\text{-}e}$, is written as follows:

$$\Omega_{c\text{-}e} = \sum_{i \in B} \omega_i e_{el,i} N_a - \sum_{r}^{R_{EI}} \omega_r I_r N_a + \sum_{r}^{R_{EI,AI}} \omega_r e_e N_a - \sum_{i}^{m} \sum_{j}^{l_i} (1 - \psi_i) \omega_{ij} D_{ij} N_a. \tag{7}$$

The first term indicates the change of the species electronic energy, with the electronic state populations assumed to follow a Boltzmann distribution. The second and the third terms are correspondingly the electron energy loss and gain due to the electron impact and associative ionization processes.

The ionization energy, I_r, is set to the value of the ionization potential of the ground state. The last term represents the electron energy loss due to electron impact dissociation, and l_i is the number of electronic states of the ith molecule.

In the modeling of the chemical reaction of the 2T-QSS model, the reaction rates of the dissociation, associative and electron impact ionization, charge, and NO exchange reactions are taken from the work of Park *et al.* [22].

In the 2T-QSS model, the set of electronic master equations of N, N_2, N_2^+, O, O_2, and NO is solved in a decoupled manner by applying the electronic QSS assumption [1]. Thus, solutions of the electronic master equations are obtained by the postprocessing of the flow field properties calculated by the conventional 2T model. This 2T-QSS model has been developed to predict instances of measured nonequilibrium radiation overshoot [23]. For a given thermodynamic condition, the electronic QSS assumption is satisfied when the rate of change of an electronic state is much smaller than both the sum of all incoming rates and the sum of all outgoing rates. This postulates that the freezing phenomenon occurs for the given electronic state. In the conventional 2T-QSS model, it is considered that the entire flow field is in such an electronically frozen state. Hence, the electronic master equations can be linearized into a set of algebraic equations with the QSS assumption, after which the level of deviation from the Boltzmann distribution is evaluated. Because the 2T-QSS approach is simple to apply and computationally efficient, it has been adopted to analyze the nonequilibrium radiative flows in various studies [3,7,9].

B. Electronic master equation coupled model for atoms

In the second model, denoted as the EM-atom model, electronic state-resolved master equation analyses of N and O are carried out in a tightly coupled manner with the flow field calculation. As a result, non-Boltzmann electronic state populations of N and O are determined without considering the electronic QSS assumption. On the other hand, the electronic state populations of N_2, N_2^+, O_2, and NO are calculated by applying the electronic QSS assumption. When calculating the flow field using the EM-atom model, the vibrational energy and the electron-electronic energy modes are separated in comparison with the conventional 2T model; these are denoted as the vibrational temperature $T_{\rm vib}$ and the electron-electronic temperature T_{eex}, respectively. The vibrational and electron-electronic energy conservation equations are then expressed as follows:

$$u\frac{\partial E_{\rm vib}}{\partial x} = \Omega_{v\text{-}T} + \Omega_{e\text{-}v} + \Omega_{c\text{-}v}, \tag{8}$$

$$u\frac{\partial E_{eex}}{\partial x} = \Omega_{e\text{-}T} - \Omega_{e\text{-}v} + \Omega_{c\text{-}e} + \Omega_{\rm EM} - \Omega_{{\rm rad},f\text{-}b}. \tag{9}$$

The electron-vibrational energy (EV) transfer rate, $\Omega_{e\text{-}v}$, is described using the Landau-Teller formula, as

$$\Omega_{e\text{-}v} = \sum_s^m \frac{E_{{\rm vib},s}(T_{eex}) - E_{{\rm vib},s}(T_{\rm vib})}{\tau_{ev,s}}. \tag{10}$$

The EV relaxation times, $\tau_{ev,s}$, of the N_2-e^- and O_2-e^- collisions are determined using the analytical fitting functions devised in the work by Lapota *et al.* [24,25]. Unlike the 2T-QSS method, I_r in Eq. (7) is set to the ionization potential of each electronic level in the present EM-atom model.

The last two terms in Eq. (9) indicate the rates of electron energy loss due to the electron impact bound-bound transition and the free-bound radiative transition. For the bound-bound transition, the rate, $\Omega_{\rm EM}$, is calculated as

$$\Omega_{\rm EM} = -\sum_r^{R_{e,b\text{-}b}} \omega_r E_r N_a, \tag{11}$$

where $R_{e,b\text{-}b}$ and E_r stand for the group of reactions and the reaction energy related to the excitation process. For the free-bound radiative transition, the energy loss rate, $Q_{{\rm rad},f\text{-}b}$, is modeled by accounting for the radiative and dielectronic recombination processes [26,27],

$$Q_{{\rm rad},f\text{-}b} = \sum_s^a \sum_j (I_s - E_j)\rho N_a^2 \gamma_{s^+}\gamma_e \times \left\{\alpha_j^{RR} K_{RR}(c,j) + \alpha_j^{DR} K_{DR}(c,j)\right\}, \tag{12}$$

where a is the group of neutral atoms, and K_{RR} and K_{DR} are the rate coefficients of the radiative and the dielectronic recombination processes, with the values taken from the work of Bourdon and Vervisch [28] and Bourdon *et al.* [29]. In the present study, the escape factor, α, is set to zero for the atomic VUV lines and one for the remaining radiative transitions to approximate the optical thickness. When the optically thick assumption is made, all of the escape factors are set to zero.

The elementary processes which induce the electronic transitions of the atoms, are the electron and heavy-particle impact excitation, the electron impact ionization, and the radiative transition. In addition, the electron and heavy-particle impact dissociation of the diatoms influences the electronic state populations of the ground and metastable states of the atoms. In the EM-atom model, the dissociation reaction is assumed to occur in the ground state, as the electronic state-to-state kinetics of the diatoms are under the electronic QSS assumption. In the present study, detailed balances [1] for the electronic bound-bound and free-bound transitions are utilized to describe the reverse processes of electron and heavy-particle impact transitions. The rates of the ith electronic concentration of the atomic species n can then be written as

$$u\frac{\partial \gamma_{n,i}}{\partial x} = \sum_{j\in{\rm N,O}} K_e(i,j)\left\{\frac{\gamma_j}{K_{E_{ij}}} - \gamma_i\right\}\rho N_a\gamma_e + \sum_{j\in{\rm N,O}}\sum_s^{\rm N,O} K_{h,s}(i,j)\left\{\frac{\gamma_j}{K_{E_{h,ij}}} - \gamma_i\right\}\rho N_a\gamma_s + K_e(i,c)\left\{\frac{\gamma_{n^+}\gamma_e}{K_{E_{ic,+}}}\rho N_a - \gamma_i\right\}\rho N_a\gamma_e + \sum_{j\in N_2,O_2}\delta_{i,k}\epsilon_{k,l}K_e^D(j,c)\left\{\gamma_j - \rho N_a\frac{\gamma_{n,k}\gamma_{n,l}}{K_{E_{jc,D}}}\right\}\rho N_a\gamma_e$$

$$+\sum_{j\in \mathrm{NO},\mathrm{N}_2^+}\left[K_e^D(j,c)\left\{\gamma_j-\rho N_a\frac{\gamma_{n,i}\gamma_m}{K_{E_{jc,D}}}\right\}\rho N_a\gamma_e+\sum_s^C K_{h,s}^D(j,c)\left\{\gamma_j-\rho N_a\frac{\gamma_{n,i}\gamma_m}{K_{E_{h,jc,D}}}\right\}\rho N_a\gamma_s\right]$$

$$+\sum_{j\in \mathrm{N}_2,\mathrm{O}_2}\sum_s^C \delta_{i,k}\epsilon_{k,l}K_{h,s}^D(j,c)\left\{\gamma_j-\rho N_a\frac{\gamma_{n,k}\gamma_{n,l}}{K_{E_{h,jc,D}}}\right\}\rho N_a\gamma_s$$

$$+\sum_{j,j>i}^{l_n}\alpha_{ji}A(j,i)\gamma_j-\sum_{j,j<i}^{l_n}\alpha_{ij}A(i,j)\gamma_i+\left\{\alpha_i^{RR}K_{RR}(c,i)+\alpha_i^{DR}K_{DR}(c,i)\right\}\rho N_a\gamma_{n^+}\gamma_e, \tag{13}$$

where $K_e(i,j)$ and $K_{h,s}(i,j)$ are the electronic bound-bound transition rates of the electron and heavy-particle impact excitation, respectively. $K_e(i,c)$ denotes the bound-free transition rates of the electron impact ionization, and K_e^D and $K_{h,s}^D$ are correspondingly the dissociation rates of diatoms induced by electron and heavy-particle collisions. The indices k and l denote the electronic states of the atomic species which are the dissociation products of homonuclear molecules in a neutral state. The symmetric factor, $\epsilon_{k,l}$, is defined as $\epsilon_{k,l}=2$ if $k=l$ or $\epsilon_{k,l}=1$ if $k\neq l$, and δ is Dirac delta function. The indices n^+ and m represent the product of ionization and the dissociation of heteronuclear molecules, respectively. K_E is the equilibrium constant, and C is the group of colliding heavy particles of N, O, N_2, O_2, and NO. The Einstein coefficient, A, indicates the probability of spontaneous emission due to the bound-bound processes, and it is taken from the NIST database [12]. In the present study, the absorption of the radiating gas is modeled by introducing the escape factor, α.

A comparison work between existing data [1,30–39] is carried out to construct the best set of electronic state-to-state rates for N and O. The electron impact excitation of atoms is one of the most dominant processes associated with the lunar return condition of interest at present. Figure 1 shows a comparison between the electron impact excitation rates

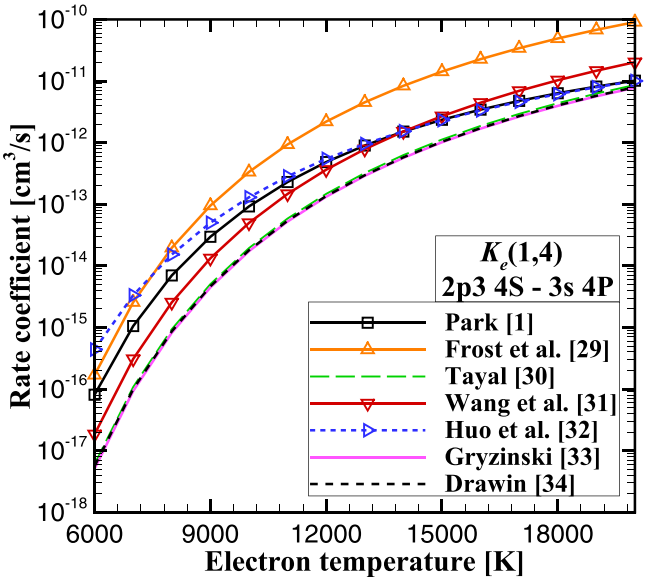

FIG. 1. Comparison of various electron impact excitation rate parameters for N of Refs. [1,30–35].

[1,30–35] for the ($i=1$, $j=4$) electronic transition of N. In previous studies by Panesi *et al.* [10] and Johnston *et al.* [40], the accuracy of CR models was improved by applying rates from Frost *et al.* [30] and Tayal [31], which were calculated by *B*-spline *R*-matrix methods instead of semiempirical formulas [1,34,35]. However, the covered electronic transitions [30,31] are not sufficient for an accurate description of the electronic population. Recently, Wang *et al.* [32] and Huo *et al.* [33] evaluated sets of cross sections by applying improved quantum mechanical methods, and their findings cover wider ranges of electronic transitions than those by Frost *et al.* [30] and Tayal [31]. As shown in Fig. 1, the electronic transition rates by Wang *et al.* [32] and Huo *et al.* [33] are well bounded between the existing transition rates [1,30,31,34,35]. Because the present atomic group levels in Table II are not compatible with the electronic states considered in work by Huo *et al.* [33], the rates by Wang *et al.* [32] are prioritized for the available electronic transitions in the present study. For the electronic transitions between the grouped levels of $n_p>27$, the empirical model proposed by Park [1] is adopted. For the other electronic transitions, the empirical formulation by Gryzinski [34] is applied for the evaluations. In the electron impact ionization transition of N, the rates proposed by Wang *et al.* [32] are employed to describe the ionization from the ground and first two metastable states. For ionization from the other electronic states, the total cross sections proposed by Ciccarino and Savin [38] are adopted to calculate the bound-free transition rates.

For O, the electron impact excitation processes are modeled by utilizing the rates proposed by Tayal and Zatsarinny [36,37] for the available electronic transitions. The data in the work of Refs. [36,37] are obtained by the *B*-spline *R*-matrix method, as was done by Wang *et al.* [32]. Similar to the electronic transition modeling of N, the empirical rates proposed by Park [1] are adopted for the electronic transitions between the grouped levels above $n_p>27$. For the remaining transitions, the empirical formula by Gryzinski [34] is applied for optically allowed transitions, and the empirical rates proposed by Drawin and Emard [35] are used for optically forbidden cases. In the ionization process, the rate coefficients by Tayal and Zatsarinny [36] are adopted for the first three states. For ionization from other electronic states, the empirical formulation by Drawin and Emard [35] is used.

During the modeling of the heavy-particle impact excitations of N and O, considerable uncertainty still exists [3,9], as a collisional transition can occur even between optically forbidden states, and some difficulty arises when attempting to obtain measured data at a high temperature. In recent work

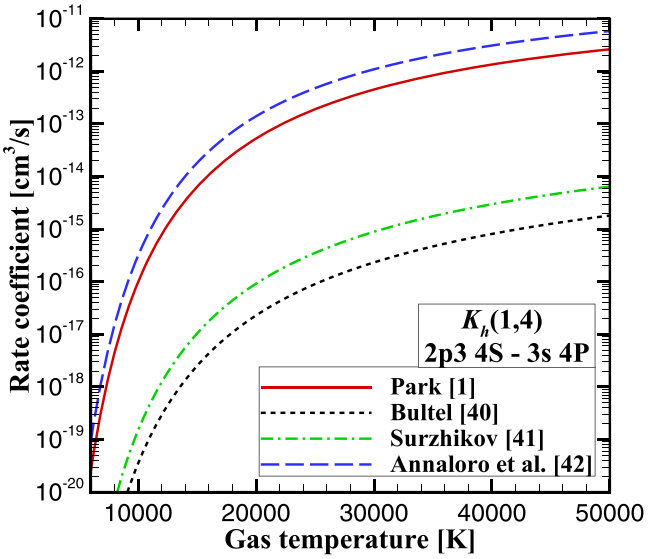

FIG. 2. Comparison of various heavy-particle impact excitation rates of N of Refs. [1,41–43].

by Lemal *et al.* [9], it was revealed that the heavy-particle impact excitation significantly affects non-Boltzmann state populations when electrons are scarce. In Fig. 2 a comparison of the existing heavy-particle impact excitation rates [1,41–43] is presented for the ($i = 1$, $j = 4$) electronic transition of N. Discernible differences are observed between the rates because they were evaluated through calibration based on existing measured data at a specific wavelength. In the present work, the empirical rates given by Surzhikov [42] are adopted for optically allowed transitions, and the cross sections proposed by Park [1] are applied for optically forbidden cases, as recommended by Lemal *et al.* [9]. The resultant set of electronic state-to-state transition rates of N and O selected in the present work is summarized in Table III.

C. Electronic master equation coupled model for air

In the third model, denoted as EM-air, the set of electronic master equations of N, N_2, N_2^+, O, O_2, and NO is simultaneously calculated together with the flow conservation equations of Eq. (1). Thus, the electronic QSS assumption is not applied when calculating the electronic populations of the atoms and molecules. In the N and O atoms, the electronic state-to-state kinetics are analogously modeled via the EM-atom method, except for the dissociation reaction. In the dissociation reaction of the EM-air model, the electronically excited atoms of the dissociation products are considered even in their ground or metastable states when Eq. (13) is numerically integrated.

The elementary processes, which induce the electronic transitions of the diatoms, are the radiative transition and the electron and heavy-particle impact excitations and dissociations. The electronic transition rates of the ith electronic concentration of the diatomic species n can be written as

$$u\frac{\partial \gamma_{n,i}}{\partial x} = \sum_j K_e(i,j)\left\{\frac{\gamma_j}{K_{E_{ij}}} - \gamma_i\right\}\rho N_a \gamma_e + \sum_j \sum_s^C K_{h,s}(i,j)\left\{\frac{\gamma_j}{K_{E_{h,ij}}} - \gamma_i\right\}\rho N_a \gamma_s + K_e^D(i,c)\left\{\rho N_a \frac{\gamma_k \gamma_l}{K_{E_{ic,D}}} - \gamma_i\right\}\rho N_a \gamma_e$$
$$+ \sum_s^C K_{h,s}^D(i,c)\left\{\rho N_a \frac{\gamma_k \gamma_l}{K_{E_{h,ic,D}}} - \gamma_i\right\}\rho N_a \gamma_s + \sum_{j,j>i}^{l_n} \alpha_{ji} A(j,i)\gamma_j - \sum_{j,j<i}^{l_n} \alpha_{ij} A(i,j)\gamma_i, \quad (14)$$

where the indices k and l represent the products of dissociation. For diatomic species, the effective Einstein coefficient is obtained from the work by Hyun [16]. In the effective Einstein coefficient, averaging of the upper vibrational states is carried out for computational efficiency. In the modeling of the associative ionization and the charge and NO exchange reactions, it is assumed that the reactions occur in the electronic ground state, following the work by Johnston and Panesi [44]. This is done due to the lack of knowledge of related rates for the air mixture. The reaction rates of the associative ionization and charge and the NO exchange reactions are taken from the work of Park *et al.* [22].

In hypersonic shock layer calculations, accurate modeling of the diatomic collisional excitation is important when analyzing the radiative heat flux behind a shock wave. In Fig. 3 a comparison of the existing electron impact excitation rates [45–51] for the (X-B) transition of N_2 is presented. The calculated transition rates [49–51] are compared with the measured data [45–48], which were determined by emission spectroscopy adopting various electron beam energies. In the calculations of the transition rates [49–51], the Franck-Condon principle [1] is adopted to describe the electronic and the vibrational transitions separately. In previous studies by Teulet *et al.* [49] and Chernyi and Losev [50], the rates for electronic excitation were evaluated using the weighted total cross section (WTCS), which presents less reliable results at high temperatures [52]. On the other hand, in the work by Park [51], the existing measured cross sections were adopted for various transitions to calculate the excitation rates. The rates proposed by Park [51] are utilized in the present study, as these are in better agreement with the measured data [45–48] compared to the other calculations [49,50], as shown in Fig. 3.

Figure 4 shows a comparison of the existing heavy-particle impact excitation rates [41–43,53] for the (X-A) transition of N_2. A significant discrepancy is observed between the electronic transition rates, similar to the atomic cases shown in Fig. 2. Given that the Franck-Condon principle is weakly in effect for this electronic transition, experimental data are definitely required to evaluate the rates accurately. However, most of the measurements were taken at room temperature. A set of heavy-particle impact excitation rates of diatoms was proposed by Park [53] while extrapolating the measured quenching cross sections at high temperatures. In previous work performed by Panesi *et al.* [26], the accuracy of the

TABLE III. Selected electronic state-to-state transition rates for N and O.

Transition	Process[a]	States	Source
Electron impact excitation	$N(i)+e^- \rightarrow N(j)+e^-$	$(i<27, j<28)$	[32]
		$(i<27, 27<j<38), (i=27, j>i)$	[34]
		$(i>27, j>28)$	[1]
	$O(i)+e^- \rightarrow O(j)+e^-$	$(i<14, j<22)$	[36,37]
		$(i>27, j>28)$	[1]
		Remaining (optically allowed)	[34]
		Remaining (optically forbidden)	[35]
Electron impact ionization	$N(i)+e^- \rightarrow N^+ + 2e^-$	$(i=1, 2, 3)$	[32]
		$(i>3)$	[38]
	$O(i)+e^- \rightarrow O^+ + 2e^-$	$(i=1, 2, 3)$	[36]
		$(i>3)$	[35]
Heavy particle impact excitation	$A(i)+M \rightarrow A(j)+M$	Optically allowed	[42]
		Optically forbidden	[1]
Radiative transition	$N(j) \rightarrow N(i<j)+h\nu$	All (219 transitions)	[12]
	$O(j) \rightarrow O(i<j)+h\nu$	All (117 transitions)	[12]

[a]A: N and O.

rates [53] was found to be reliable for application to hypersonic conditions. Thus, the heavy-particle impact excitation rates proposed by Park [53] are prioritized for the available electronic transitions in the present study. For the electronic transitions which were not considered in the work by Park [53], the semiempirical formula derived by Annaloro *et al.* [43] is utilized in the present study.

The electronic state-resolved dissociation rates by the electron and heavy-particle impact processes are obtained from the database proposed by Park [51,53]. The present resultant set of electronic state-to-state transition rates for N_2, N_2^+, O_2, and NO is summarized in Table IV. The compilations of the electronic transition rates for the atoms and diatoms presented in Tables III and IV are equally applied to the three-physical models of 2T-QSS, EM-atom, and EM-air for consistency.

D. Radiation analysis

Radiative properties are calculated in spectral ranges to predict measured nonequilibrium radiation in a shock tube. In the present study, a line-by-line method is devised to conduct the spectral calculations. For the atomic species, the bound-bound, bound-free, and free-free transitions are modeled. The atomic line data are obtained from the NIST (v5.4) database [12]. In the calculations of the bound-free transition, the curve fit of Johnston [54] based on the TOPbase [55] is utilized here. In the free-free transition, the absorption cross section is taken from the work by Peach [56]. In addition to the bound-free and the free-free transitions of the neutral atoms, the continuum radiation by the photodetachment of atomic negative ions is also considered. The cross sections required to evaluate the continuum radiation are taken from various sources [57–59]. For the diatomic species, the bound-bound

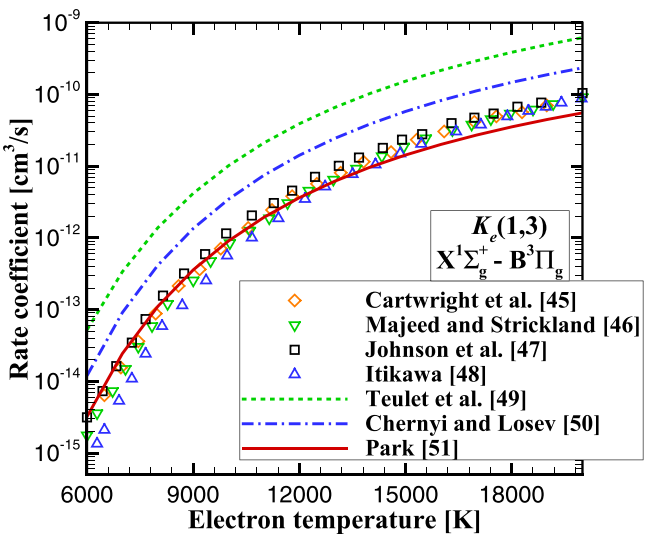

FIG. 3. Comparison of various electron impact excitation rate parameters for N_2 of Refs. [45–51].

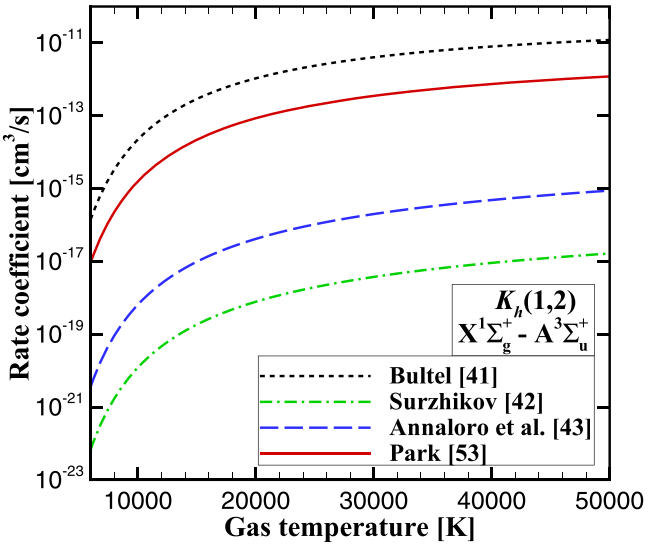

FIG. 4. Comparison between heavy-particle impact excitation rate parameters for N_2 of Refs. [41–43,53].

TABLE IV. Selected electronic state-to-state transition rates for the diatoms.

Transition	Process[a,b]	Source
Electron impact excitation	$A(i)+e^- \rightarrow A(j)+e^-$	[51]
Electron impact dissociation	$A(i)+e^- \rightarrow A_1(j_1)+A_2(j_2)+e^-$	[51]
Heavy particle impact excitation	$A(i)+M \rightarrow A(j)+M$	[43,53]
Heavy particle impact dissociation	$A(i)+M \rightarrow A_1(j_1)+A_2(j_2)+M$	[53]
Radiative transition	$A(j) \rightarrow A(i<j)+h\nu$	[16]

[a] A: N_2, N_2^+, O_2, and NO.
[b] A_1 and A_2: dissociation products.

transition is modeled. The radiative transition probabilities within the rovibronic states and the Franck-Condon factor employed to calculate the averaged electron-impact excitation rates are taken from the work of Hyun [16]. At the strongest vibrational bands in the N_2 VUV systems, the electronic-vibrational transition moment, $R_e^{v'v''}$, calculated by Chauveau *et al.* [15], is utilized instead of the data by Hyun [16] due to the lower level of uncertainty of the former data [8]. The effects of physical line broadening are modeled by applying the Voigt line profile [60], which includes the mechanisms of the Doppler, natural, pressure, and Stark broadenings.

Spatial distributions of the spectrally resolved radiance can be calculated as

$$I(x,\lambda) = S(x,\lambda)(1-e^{-\kappa(x,\lambda)D}), \tag{15}$$

where S is the source function, defined as the ratio of the emission coefficient to the absorption coefficient, κ. Also, D and I are the diameter of the driven tube and the spectral intensity along the distance x, respectively. The radiating medium is assumed as a uniform state along the line of sight. The total smearing function [4] including the ILS and SRF is applied to make comparisons between the calculated and the measured intensity. With the ILS, the spectrally smeared intensity, J, can be written as [9]

$$J(x,\lambda) = \int_{-\infty}^{+\infty} I(x,\lambda)\Phi_{\mathrm{ILS}}(\lambda-\lambda')d\lambda', \tag{16}$$

where Φ_{ILS} is the ILS function. In the work by Brandis and Cruden [4], the form of Φ_{ILS} was determined by fitting the measured atomic lines, which were emitted from a calibration lamp. The resolution of the optical setup, the charge sharing of the spectrometer, and the motion of the shock during the camera acquisition all influence the spatial resolution of the measured intensity distribution. With the SRF, the spatially smeared intensity [61], R, is calculated as

$$R(x) = \int_{-\infty}^{+\infty}\int_{\Delta\lambda} J(x,\lambda)\Phi_{\mathrm{SRF}}(x-x')\,d\lambda\,dx', \tag{17}$$

where Φ_{SRF} is the SRF function. The parameters required to determine the forms of Φ_{ILS} and Φ_{SRF} are taken from an online database [6]. By applying Eqs. (16) and (17) to Eq. (15), the smeared intensity distributions measured from the experiments can be reproduced in the x-λ domain. In the analysis of the measured data, the shock front location is important for an accurate spatial analysis. In the present study, it is determined by taking the tangent to the measured intensity profiles.

III. POSTSHOCK FLOW AND RADIATION CALCULATIONS

The nonequilibrium radiative transitions occurring behind strong shock waves depend on certain physical conditions, such as the shock speed, the freestream pressure, and the wavelength range considered. Therefore, various flow conditions should be considered when validating the accuracy of the present physical models by comparisons with measured nonequilibrium radiation levels.

In the present study, four different flow conditions of EAST shock tube experiments are considered in the analysis of nonequilibrium radiative transitions of high-enthalpy flows. The flow conditions of the EAST shock tube experiments are summarized in Table V. The Cases 1 and 2 represent the condition of entering flight from a low-earth orbit. The flow conditions of Cases 3 and 4 represent peak heating for the reentry of a multipurpose crew vehicle.

Because each electronic state is considered as a single species, the electronic state-resolved analysis of the air plasma flows is computationally very demanding. A parallel computing technique based on PC-based Linux clusters is used to enhance the computational efficiency without any loss of accuracy. In solving the governing equations of the developed postshock flow solver, an implicit integration method [62] is applied to improve the stability of the calculation.

A. Case 1 of 8.18 km/s and 0.01 Torr

Because massive dissociation does not occur in the flow condition of Case 1, the majority of the radiation is emitted from the diatomic molecules, in this case N_2, N_2^+, O_2, and NO. Therefore, the diatomic CR transitions must be investigated in detail. In Fig. 5 the calculated temperature and number density distributions using the present physical models of the 2T-QSS and EM coupled models of EM-atom and EM-air are presented. In Case 1, thermochemical equilibrium cannot be

TABLE V. Considered flow conditions of the EAST shock tube experiments.

Condition	Case 1	Case 2	Case 3	Case 4
Shock velocity, km/s	8.18	8.57	10.68	11.17
Initial pressure, Torr	0.01	0.01	0.2	0.1
Wavelength, nm	190–440	500–1450	119–180	856–872
EAST shot number	59–15	59–32	50–93	50–119
Source	[3]	[3]	[4]	[4,9]

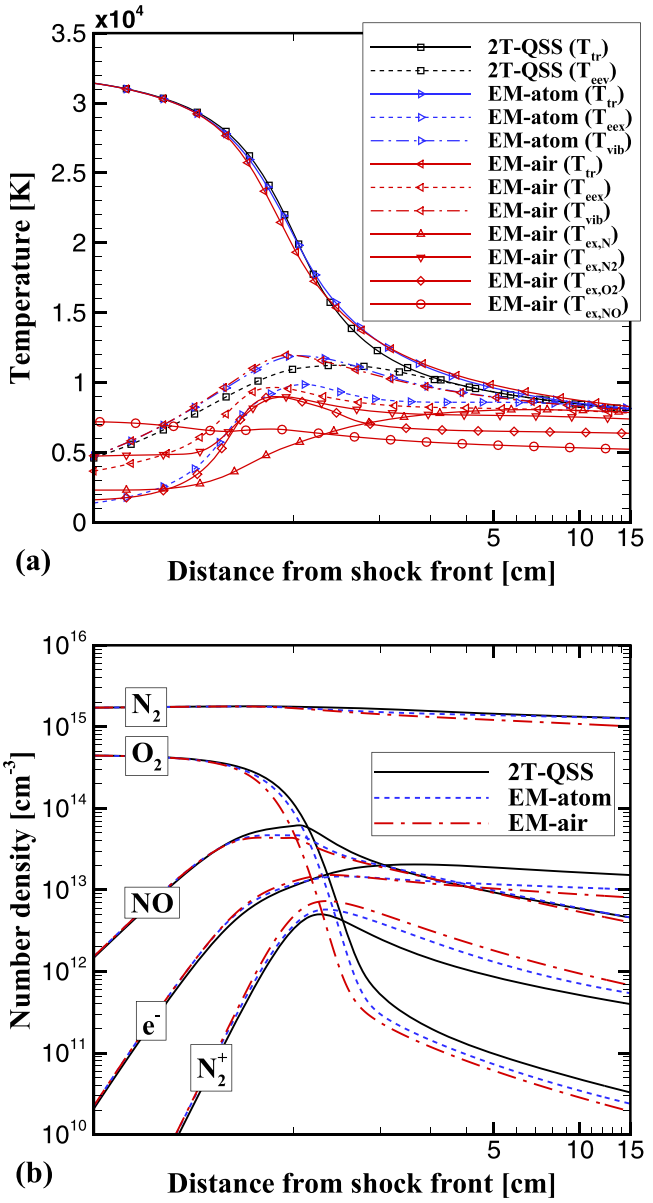

FIG. 5. Comparison of the calculated (a) temperature and (b) number density profiles for the condition of Case 1.

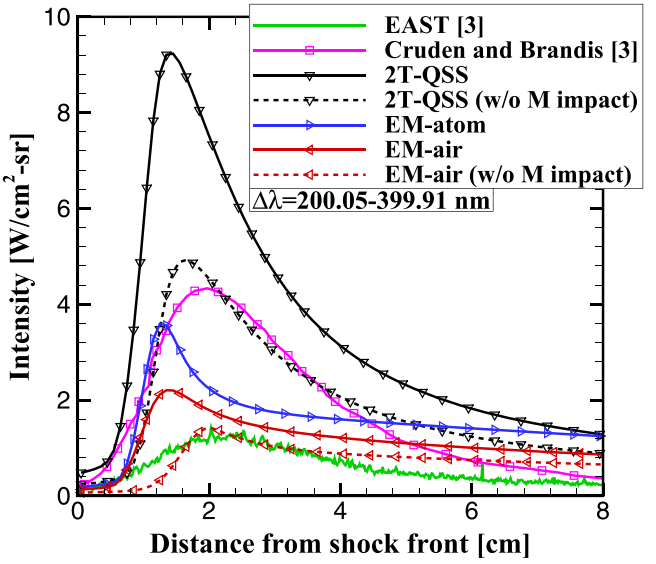

FIG. 6. Comparison of the calculated intensity profiles with the EAST measurement [3] for the condition of Case 1.

achieved due to the extremely low pressure of the freestream. The thermochemical relaxations of the EM coupled models occurred more slowly than those of the 2T-QSS model, as shown in Fig. 5(a). This arose because the bound-bound collisional excitation source term, Ω_{EM}, in Eq. (9) has a negative sign. The associative ionization governs the production of free electrons, and it ionizes the species near the shock front. Thus, the initial rising rate of the N_2^+ excitation temperature, T_{ex,N_2^+}, is nearly identical to the electron-electronic temperature of EM coupled models. Behind a strong shock wave, the electron translational temperature rules the radiative transition, and the predicted free electron translational temperature of the 2T-QSS model is higher than those in the EM coupled models. In the EM coupled models, the difference between vibrational and electron-electronic temperatures is approximately 3000 K at a maximum. In the downstream of $x = 2$ cm, the amount of free electrons calculated by the 2T-QSS model is larger than those by the EM coupled models, as shown in Fig. 5(b). This aspect influences the absolute radiation intensity distribution, as a free electron is a highly efficient collider which leads to CR transitions.

Figure 6 shows a comparison of the spatial intensity profiles in the UV range. In previous work by Cruden and Brandis [3], the flow field was calculated using a 2T model. Then the non-Boltzmann state populations were evaluated by applying the electronic QSS assumption. This is an approach similar to the present 2T-QSS model. The initial rising rate of the measured intensity near $x = 0.5$ cm and the radiation peak are more accurately predicted by the present EM coupled models in comparison with the 2T-QSS model. In the 2T-QSS model, the calculated results overestimate the measured peak values because the electron translational temperature calculated by the present 2T-QSS model is relatively high in comparison with those by the EM coupled models, as shown in Fig. 5(a). Thus, the radiative transition and the electron impact excitation amounts according to the 2T-QSS model are larger than those by the EM coupled models. This aspect indicates that the vibrational and the electron translational temperatures should be described separately to improve the accuracy of a nonequilibrium radiation prediction. In Fig. 6 the electronic excitations with and without heavy-particle impact processes are also compared in the 2T-QSS and EM-air models. The intensity distributions change significantly due to the influence of the heavy-particle impact transitions. The intensity increment of the 2T-QSS model is much larger than that of the EM-air model, despite the fact that an identical set of rate parameters for the heavy-particle impact is applied. These aspects imply that a large amount of uncertainty still exists in the modeling of heavy-particle impact excitation phenomena. The result by the EM-air model shows better agreement with the measured data than the EM-atom model. The decay of the measured intensity in the downstream after the peak position is greater than those by the 2T-QSS and EM

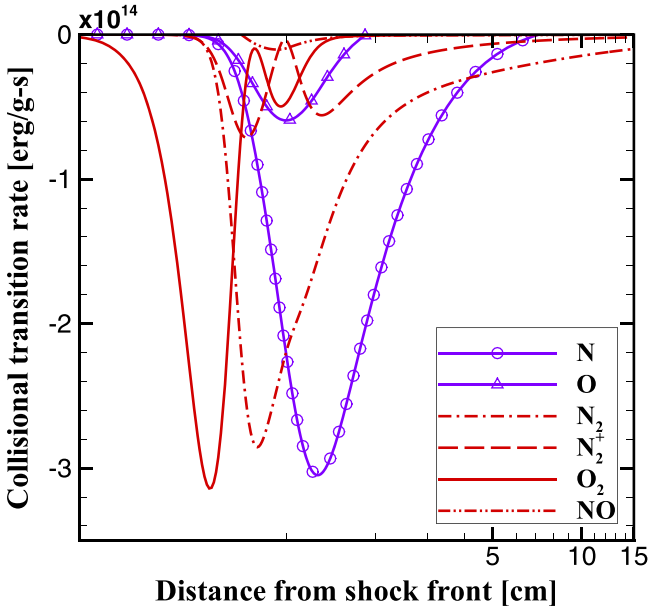

FIG. 7. Distributions of Ω_{EM} for the six considered species.

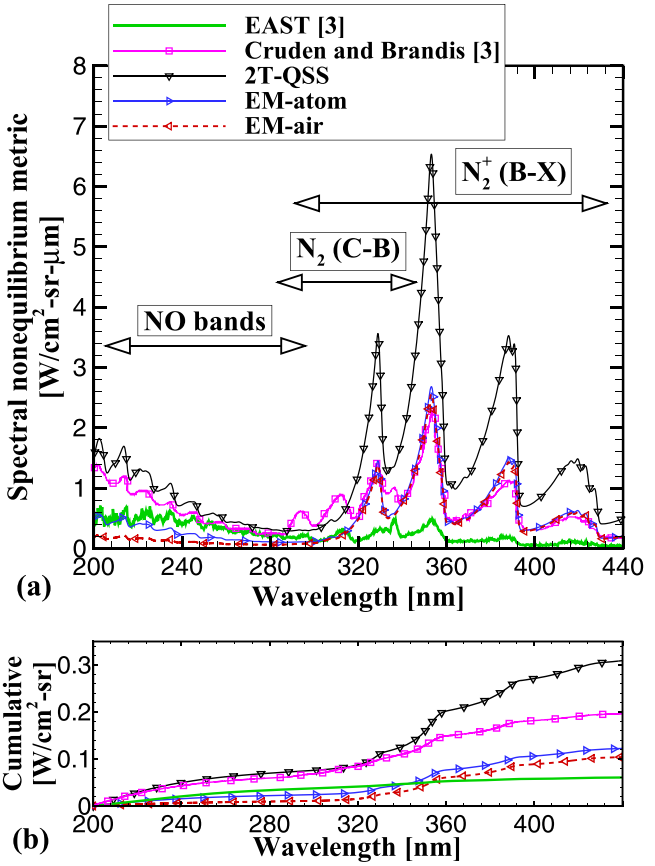

FIG. 8. Comparison of the calculated (a) spectral nonequilibrium metric and (b) cumulative nonequilibrium metric with the EAST measurement [3] for the condition of Case 1.

coupled models of EM-atom and EM-air. This is attributed to unknown radiative cooling mechanisms in the flow field.

Under the flow condition of Case 1, diatomic molecules govern the nonequilibrium processes because less dissociation occurs compared to those in Cases 3 and 4. As a result, the modeling of the excitation and dissociation processes of the diatoms becomes a critical factor influencing the predictive accuracy. Figure 7 shows the calculated distributions of Ω_{EM} for the six species of N, N_2, N_2^+, O, O_2, and NO by the EM-air model. Interestingly, the orders of the energy loss rate by collisional bound-bound transitions are comparable between the atoms and the diatoms. This indicates that the electronic master equations of the diatoms should be considered together with those of the atoms when the electronic state-to-state kinetic approach is developed.

The concept of a nonequilibrium metric was introduced by Brandis *et al.* [61] to identify the benchmark of EAST shots. This quantity is calculated by integrating the intensity within 2 cm of either side of the peak position. The nonequilibrium characteristics can be investigated in detail using this parameter. In Fig. 8 comparisons of the spectral nonequilibrium metrics are presented. In the given spectral range, the second positive (C-B) of N_2, first negative (B-X) of N_2^+, and γ (A-X) and the β (B-X) bands of NO are the possible contributors of molecular radiation. As shown in Fig. 8(a), the N_2^+ (B-X) system is the dominant influence in the spectral range of 320–440 nm under the flow condition of Case 1. All physical models considerably overestimate the N_2^+ radiation. The spectral nonequilibrium metric is more accurately predicted by the EM coupled models of EM-atom and EM-air compared to that by the 2T-QSS model in the 300–440 nm range. The higher electron translational temperature of the 2T-QSS model induces the overestimation of the radiance. The results by the EM coupled models are similar to that by Cruden and Brandis [3] for the prediction of the N_2^+ (B-X) radiation. In the work by Cruden and Brandis [3], the framework of the 2T-QSS method was utilized, but some calibrations of the chemical reaction parameters for the excitation of N_2^+ were made based on measured data from the literature [63–65]. For the N_2 (C-B) radiation, the EM coupled models are in better agreement with the measured data compared to the 2T-QSS model. The EM coupled models underestimate the NO radiation in the 200–280 nm range, whereas the 2T-QSS methods overestimate the radiance. In earlier work [3], the chemical reaction rates pertaining to the formation of NO, in this case the heavy-particle impact excitation and the exchange and dissociation reactions, were altered to enhance the modeling accuracy. Nevertheless, considerable uncertainty in the modeling of the diatomic radiations remains. Therefore, further study is clearly required for nonequilibrium cases of N_2^+ and NO. As shown in Fig. 8(b), the EM coupled models represent better agreement with the measured cumulative radiance compared to the 2T-QSS results.

In Fig. 9 comparisons of the calculated distributions of the N_2^+ (X, B) and N_2 (B) state populations are presented. The upper state populations of the N_2^+ (B-X) system are comparable among the three models of 2T-QSS, EM-atom and EM-air. The EM-air model predicts the largest ground state population. As a result, the lowest amount of radiative emission is calculated, as shown in Fig. 8(a). Although the radiation by the N_2 (C-B) system is not dominant in the given flow condition, the calculated absorbing state populations are

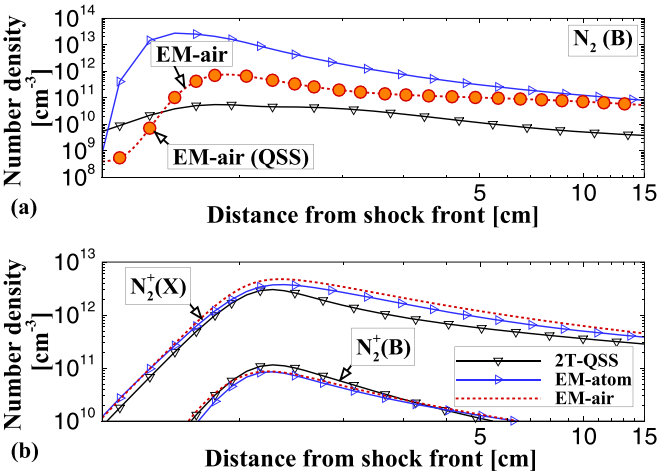

FIG. 9. Comparisons of the calculated state population distributions of (a) N_2 (B) and (b) N_2^+ (X, B) for the condition of Case 1.

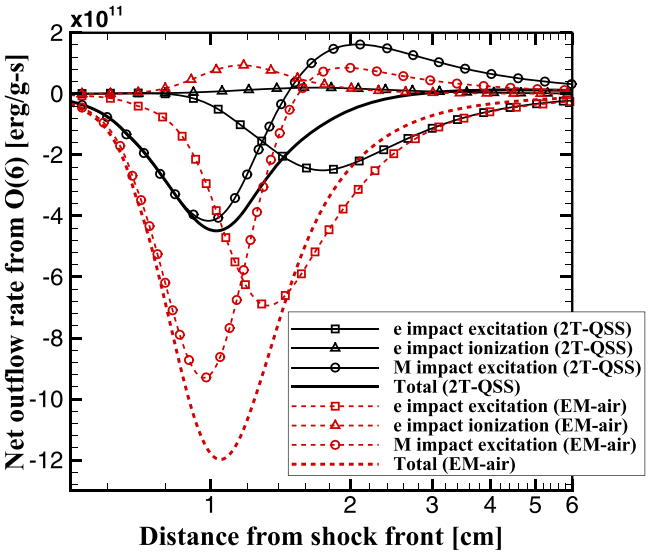

FIG. 11. Distributions of the net outflow rate from O(6).

compared in Fig. 9(b). It was found that the electronic QSS assumption appeared to be valid for the N_2 (B) state once the flow field is determined. This occurs because the electronic state population obtained by the EM-air model with the electronic QSS assumption is in good agreement with the EM-air result. However, the diatomic EM without the electronic QSS assumption significantly changes the distributions of the electronic state population. As a result, the number density of N_2 (B) by the EM-air model differs by up to one order of magnitude from those by the 2T-QSS and the EM-atom models. This aspect indicates that both atomic and diatomic EM should be coupled with the conservation equations of Eq. (1) under flow conditions where diatomic CR transitions are dominant.

B. Case 2 of 8.57 km/s and 0.01 Torr

The flow condition of Case 2 is similar to that of Case 1. Because the atomic radiation is relatively weak in this condition, the sensitivity of the 2T-QSS and EM coupled models of EM-atom and EM-air for predictions of relatively low levels of atomic CR transitions can be investigated. Figure 10 shows comparisons of the intensity profiles in the wavelength range from 530 nm to 890 nm. As shown in Fig. 10(a), the EM coupled models represent better agreement with the measured data when simulating atomic line radiation compared to the 2T-QSS results. The 2T-QSS model underestimates the atomic radiative emissions. The strongest line within the considered wavelength range is emitted from atomic oxygen at 777 nm. The EM coupled models overestimate the radiance, whereas the 2T-QSS methods underestimate it. For a comparison with the electronic population mechanism of the upper level of the O (777 nm) line, the spatial distributions of the net outflow rate from the O(6) state calculated by the 2T-QSS and EM-air models were determined, as presented in Fig. 11. The electron and heavy-particle impact excitations are the dominant transitions in the O (777 nm) line. The overall population mechanism trends by the 2T-QSS and EM-air models are similar to each other. The negative sign of the net outflow rate indicates that the inflow rate amount from the lower states due to the excitations is larger than that of the outflow rate to the higher states from O(6). The total magnitude of the quantity is larger in the EM-air model than in the 2T-QSS model. This indicates that the O(6) state is more populated in the calculations by the EM-air model. As a result, stronger

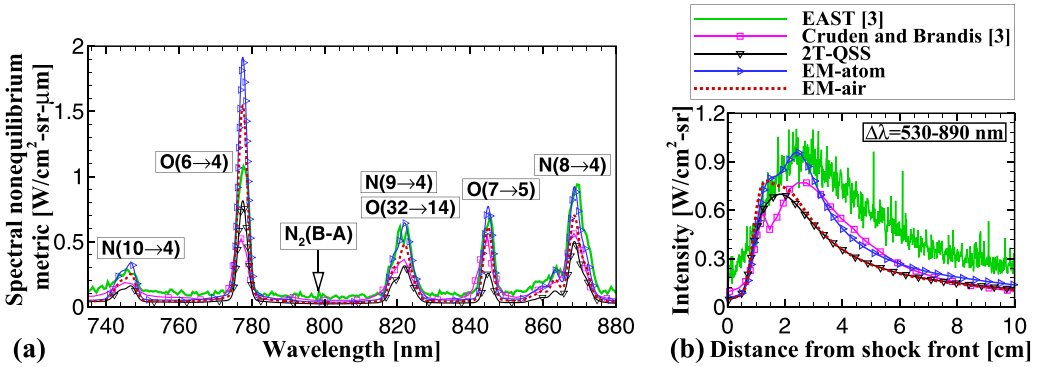

FIG. 10. Comparisons of the calculated (a) spectral nonequilibrium metric and (b) spatial intensity distributions with the EAST measurement [3] in the 530–890 nm range.

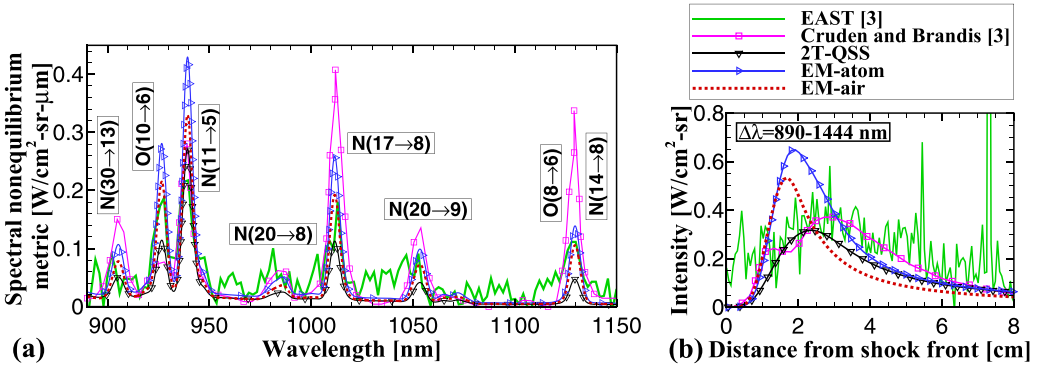

FIG. 12. Comparisons of the calculated (a) spectral nonequilibrium metric and (b) spatial intensity distributions with the EAST measurement [3] in the 890–1444 nm range.

line intensity at 777 nm is predicted by the EM-air model compared to the 2T-QSS model, as shown in Fig. 10(a).

As shown in Fig. 10(b), the EM-atom model more accurately predicted the peak of the spatial intensity than the other models. Downstream of the peak, all of the physical models slightly underestimate the decaying intensity. This can be attributed to the underestimation of the N_2 (B-A) radiation for the background emission, as shown in Fig. 10(a).

Figure 12 shows comparisons of the intensity profiles in the wavelength range from 890 nm to 1444 nm. The results by the EM coupled models of EM-atom and EM-air show better agreement with the measured intensity than those by the 2T-QSS model, except for the line of the N ($11 \rightarrow 5$) transition at 939 nm. Additionally, the EM-air model more accurately predicts the atomic lines than the EM-atom model. A previous study [3] with the 2T-QSS model overestimated most of the atomic line intensities, whereas the present 2T-QSS approach underestimates them. The prediction accuracy levels of the 2T-QSS and EM coupled models deteriorate due to an unknown radiation mechanism in the considered wavelength range. Thus, additional investigations of the nonequilibrium in the wavelength region from 890 nm to 1444 nm are required. As shown in Fig. 12(b), the spatial intensities are slightly overestimated by the EM coupled models near the shock front. This indicates that a large amount of uncertainty still exists when modeling heavy-particle impact excitations of atoms.

C. Case 3 of 10.68 km/s and 0.2 Torr

In Case 3, the freestream shock speed and pressure increase in comparison with Cases 1 and 2. In this condition, the atomic radiation becomes more important than that of the diatoms, as most diatoms are dissociated. Because the atomic emission from the VUV range has a high frequency, it significantly contributes to the radiative heating of a reentry vehicle. Therefore, a CR model must accurately predict the state populations related to radiative transitions in this wavelength region.

In Fig. 13 the calculated temperatures and species number densities of the 2T-QSS and EM coupled models of EM-atom and EM-air are presented. The result by the EM-air model is similar to that by the EM-atom model due to the rapid dissociation. The electron-electronic-vibrational temperature of the 2T-QSS model exists between the electron-electronic and the vibrational temperatures of the EM coupled

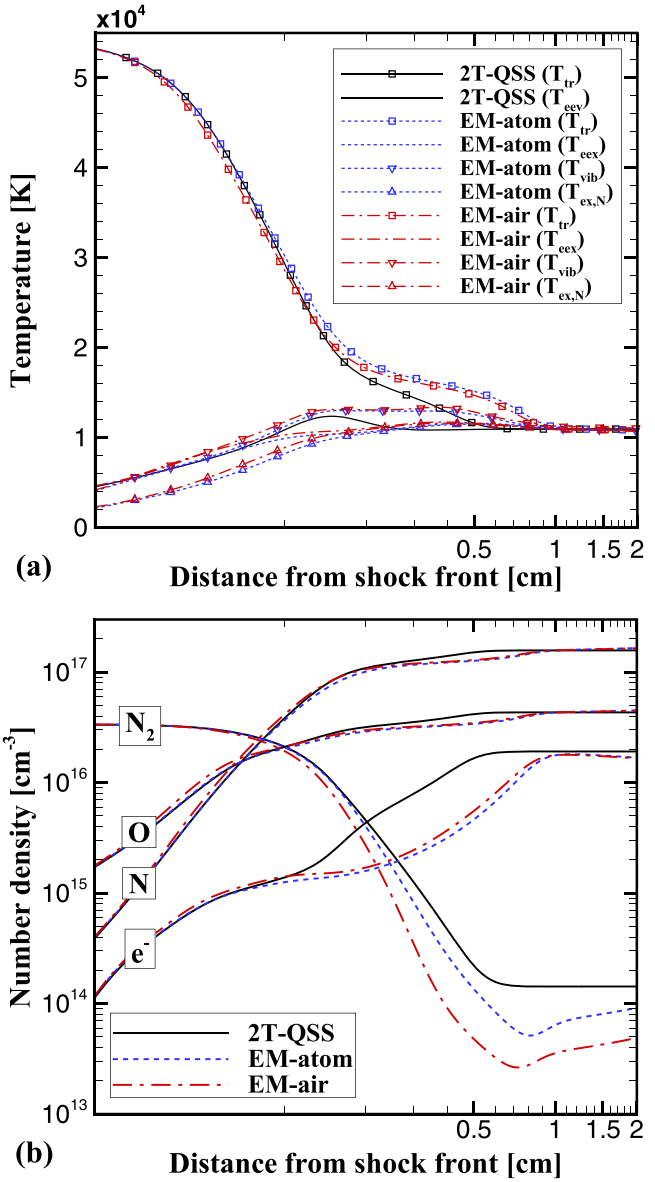

FIG. 13. Comparison of the calculated (a) temperature and (b) number density profiles for the condition of Case 3.

models. Moreover, the electron-electronic-vibrational temperature of the 2T-QSS model is higher than the electron-electronic temperature of the EM coupled models. This indicates that the ET energy exchange of the 2T-QSS model occurs more rapidly than that of the EM coupled models. In Fig. 13 it is also shown that the onset of the chemical reaction by the EM coupled models is delayed compared to that in the 2T-QSS model. This difference is partially caused by the treatment of the chemistry-electron-electronic energy coupling in Eq. (7). The contribution of the second term in Eq. (7) is overestimated near the shock front in the 2T model. This arises because the ionization potential of the ground state is assumed to be the activation energy for electron impact ionization. Unlike the 2T-QSS model, state-specific ionization potentials are employed in the EM coupled models; thus, the ionization of each state is modeled more rigorously in the EM coupled models. The number densities of N and O obtained by the EM coupled models continuously increase after thermal equilibration, as shown in Fig. 13(b), as the assumption of optically thin is applied for the radiative and the dielectronic recombination processes. Therefore, the free-bound transitions to the ground and metastable states reach their maximum levels.

Figure 14 shows comparisons of the normalized atomic state populations at $x = 0.15$ cm predicted by the three models of the 2T-QSS model and the EM coupled models of EM-atom and EM-air. In order to preserve physical consistency, optically thick calculations are performed in the EM-atom and EM-air models because, in the 2T-QSS model, the influence of radiative cooling is not considered. Under the given conditions, the excited atomic states of the EM coupled models are highly depopulated from the Boltzmann distributions due to the CR transitions. The 2T-QSS model predicts larger excited state populations than those by the EM coupled models for both N and O.

In Fig. 15 a comparison of the spatial intensity profiles is presented in the VUV range of 122-177 nm for the flow condition of Case 3. The rising rate of the intensity near the shock front is accurately predicted by the EM coupled models of EM-atom and EM-air. The 2T-QSS model also estimates the rising rate reasonably but fails to determine the proper starting position of the intensity increment. In the upstream of $x = 2$ cm, the 2T-QSS model predicts a greater intensity levels than the EM coupled models because the excited state populations as well as the electron translational temperature of the 2T-QSS model are higher than those of the EM coupled models. Furthermore, the 2T-QSS model somewhat underestimates the thermochemical relaxation time compared with the EM coupled models, as shown in Fig. 13. Under the given flow condition of Case 3, the increment of the measured intensity due to the heavy-particle impact excitation of the atoms in the region of 1.0–1.4 cm is well predicted by the EM coupled models. As stated in Sec. II, it is assumed that the escape factor is set to zero for the atomic VUV lines and one for the remaining radiative transitions. This assumption has been applied in previous studies as well [9,66], and it is a basic assumption adopted in work on radiative transitions. However, the validity of the approximation has not been investigated. In the present study, the validity of the assumption is examined. As shown in Fig. 15, the EM-atom and EM-air models

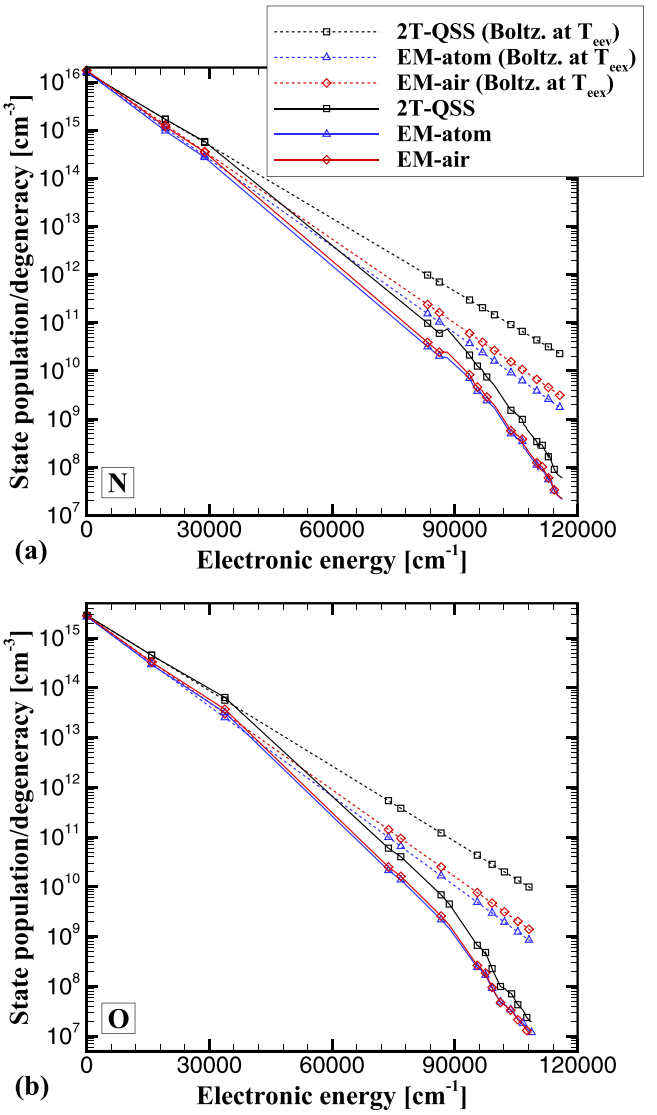

FIG. 14. Comparison of the normalized state populations of (a) atomic nitrogen and (b) atomic oxygen at $x = 0.15$ cm.

adopting this assumption fail to reproduce the intensity distribution in the equilibrium region. Moreover, the EM-atom and EM-air models with the optically thick assumption for all radiative transitions overestimate the intensity. This indicates that the process of energy loss by radiation should be modeled more rigorously instead of setting the escape factor as a constant.

Figure 16 shows comparisons of the calculated equilibrium spectral intensity and spectral nonequilibrium metrics with the EAST measurement [4]. Given the better agreement with the measured data obtained in the equilibrium region by adopting the optically thick assumption, as shown in Fig. 15, this assumption is also employed in the calculations of the equilibrium spectral intensity and spectral nonequilibrium metric. Most of the measured atomic lines exist between the results by the EM coupled models and the 2T-QSS model, except for the lines at $\lambda = 122.5$ and 122.8 nm. These exception lines represent the electronic transitions between N(29) and N(3) of the present electronic grouping levels. Although a slight

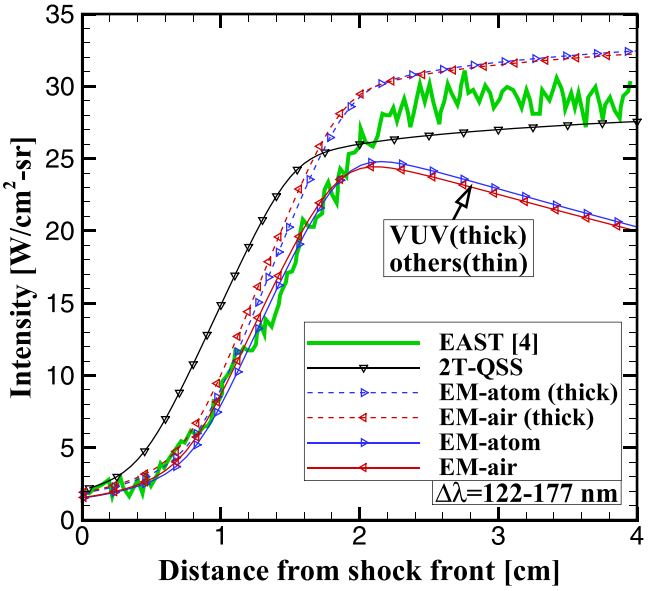

FIG. 15. Comparison of calculated intensity profiles with the EAST measurement [4] for the condition of Case 3.

discrepancy exists, it is found that the EM coupled models are well established when accurately estimating the spectral distributions of the equilibrium as well as the nonequilibrium radiation.

D. Case 4 of 11.17 km/s and 0.1 Torr

In Fig. 17 the calculated temperature and number density distributions using the three models of the 2T-QSS model and the EM coupled models of EM-atom and EM-air are compared. In Case 4, because the reaction speed of dissociation is fast under this high-speed condition, the effect of the atomic excitation is dominant, similar to the condition of Case 3. On the other hand, the relaxation time to reach thermal equilibrium is longer than that in Case 3, as the freestream pressure of Case 4 decreased to half of the pressure in Case 3. The thermochemical relaxation time of the EM-atom model is longer than that of the EM-air model because the electronic QSS assumption is applied for the diatomic species in the EM-atom model.

In Fig. 18 the calculated electron number density distributions are compared with the estimated data [9] based on the EAST measurement [4]. Under the high-speed condition, the free electron is the most effective collider given electronic excitation and ionization. Thus, an accurate prediction of the free electron number density is important when analyzing nonequilibrium phenomena. In previous work [9], the atomic nitrogen line at $\lambda = 411$ nm was used to convert the measured Stark broadening width into the electron number density. Because a simple approximate formula was employed for this conversion in that previous study [9], the uncertainty of the estimated data is considerable. Specifically, the level of uncertainty at the peak position of $x = 1.8$ cm appears to be excessive. As shown in Fig. 18, the results by the EM coupled models are in reasonably good agreement with the estimation, particularly for the prediction of the increment rate and the radiative cooling. However, in the 2T-QSS model, the initial

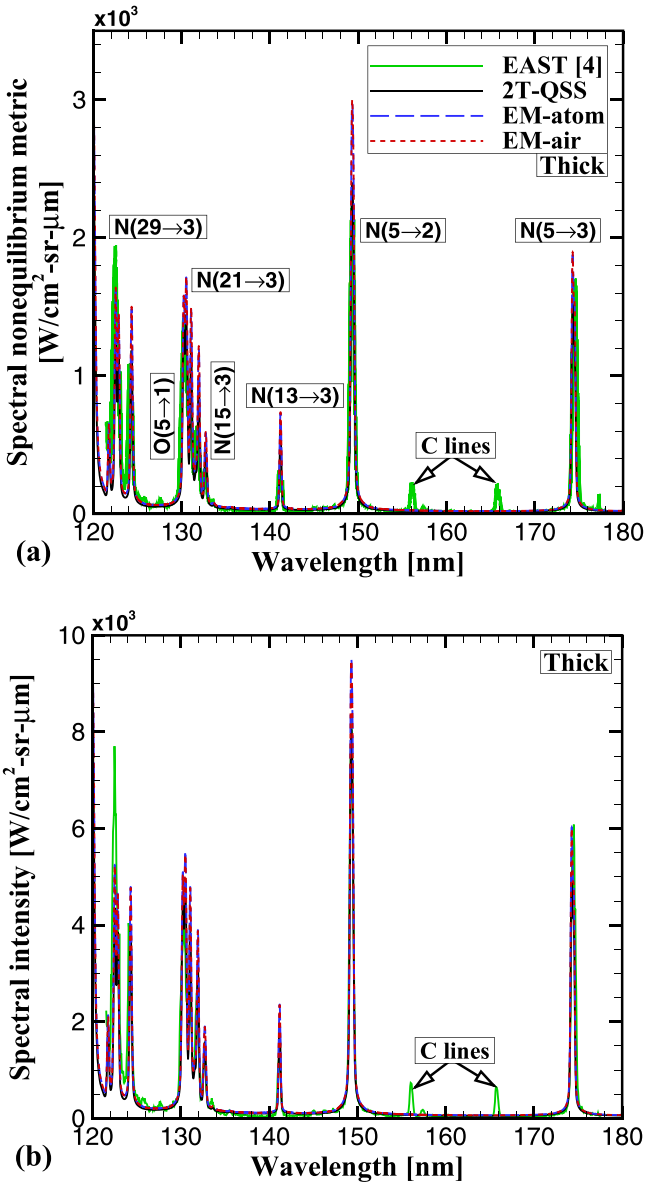

FIG. 16. Comparisons of the calculated (a) spectral nonequilibrium metric and (b) equilibrium intensity with the EAST measurement [4].

rising rate of the electron number density is significantly overestimated. These results show that the 2T-QSS model is limited in its ability to estimate the nonequilibrium status accurately under high-enthalpy flows.

As the shock speed increases, the atomic transitions significantly contribute to the spectral distributions in the near-infrared (NIR) range. The accuracy of the present models is investigated further in a comparison with EAST measurements in the NIR range. Figure 19 shows a comparison between the calculated intensity profiles and the EAST measurement [4] for the NIR wavelength range of 857-872 nm. It should be noted that proper information regarding the forms of Φ_{ILS} and Φ_{SRF} for the conditions of Case 4 was not presented in the literature [4,6]. Thus, an approximation is made to determine Φ_{ILS} and Φ_{SRF} by referring to the parameters of another test shot for similar flow conditions. This may

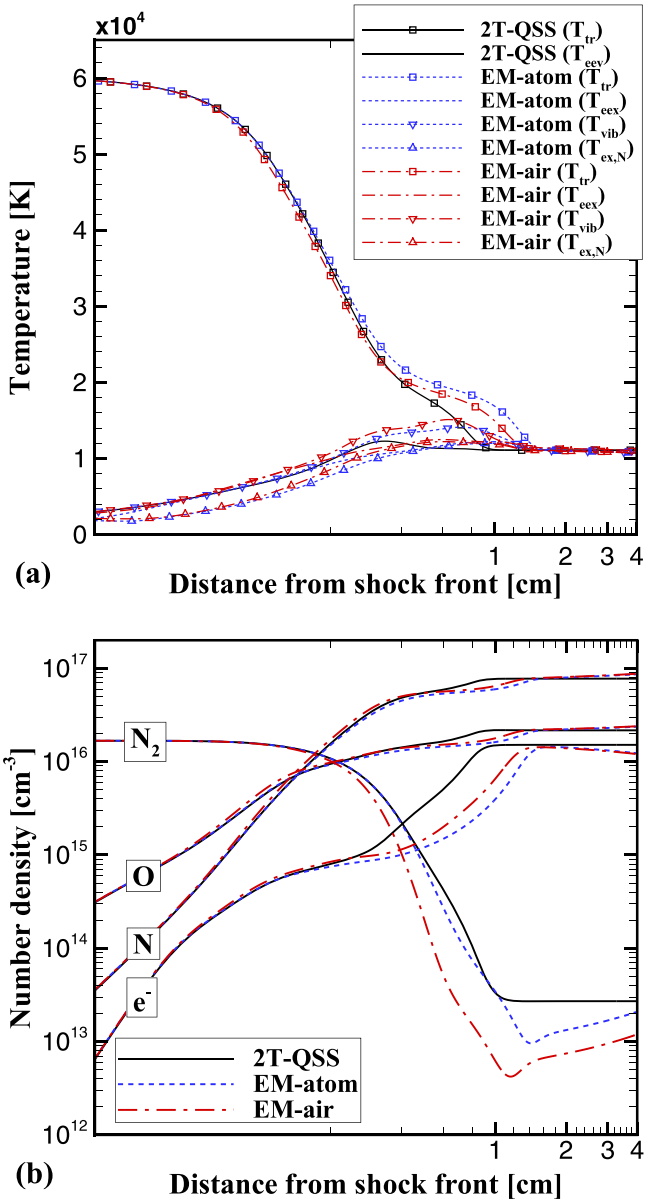

FIG. 17. Comparison of the calculated (a) temperature and (b) number density profiles for the condition of Case 4.

cause a slight discrepancy between the calculations and the measurement, particularly near the shock front. As shown in Fig. 19, the influence of the atomic heavy-particle impact excitation becomes dominant in the region of 0.5–1.5 cm because free electrons are relatively scarce. Recently, the effects of atomic heavy-particle impact excitation were investigated by Lemal *et al.* [9] based on the framework of the 2T-QSS model. In this work, it was found that the existing rate parameters cannot easily reproduce the measured intensity profiles successfully near the shock front. Thus, an arbitrary adjustment of the rate parameters of the atomic heavy-particle impact excitation was made by Lemal *et al.* [9]. Interestingly, the intensity profiles calculated by the EM coupled models of EM-atom and EM-air agree with the measured profile, as shown in Fig. 19, indicating that the heavy-particle impact excitation of the atoms is well predicted by the EM coupled

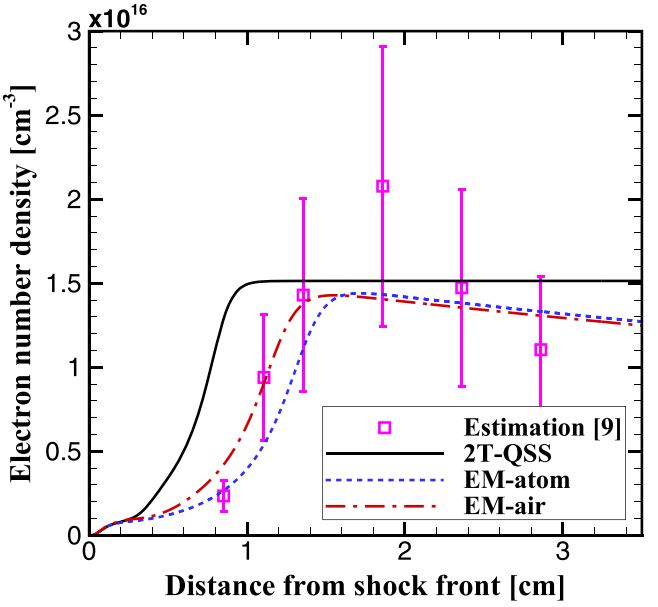

FIG. 18. Comparison of the calculated electron number density distributions with the estimated data [9] based on the EAST measurement [4].

models without modification of the rate parameters. It is also observed that the result by the EM-air model shows closer agreement with the measurement than that by the EM-atom model, as the electronic populations of the molecules are evaluated with the electronic QSS assumption in the EM-atom model. However, in the 2T-QSS model, the initial rising rate and the equilibrium value of the intensity are overestimated. In comparisons of intensity profiles with and without heavy-particle impact excitation, it was found that proper modeling of the heavy-particle impact process is mandatory for an analysis of high-enthalpy air plasma flows because the calculated

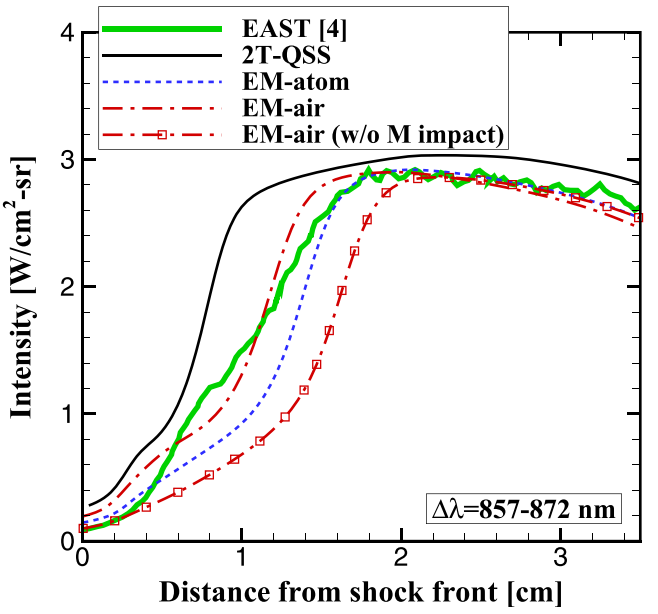

FIG. 19. Comparison of calculated intensity profiles with the EAST measurement [4] for the condition of Case 4.

relaxation time varies considerably according to the modeling of the heavy-particle impact process.

IV. CONCLUSIONS

In the present study, three different electronic state-to-state methods are devised to analyze air plasma flows in nonequilibrium states: the conventional two-temperature model with the electronic quasi-steady-state assumption (2T-QSS) and the electronic master equation coupled model for the atom (EM-atom) and for the atom and molecule (EM-air). State-of-the-art collisional-radiative transition rates for air species are newly compiled by making comparisons with existing data. Predictions of the measured nonequilibrium radiation are made for four different flow conditions in recent electric-arc shock tube experiments covering wavelengths ranging from the deep vacuum ultraviolet (VUV) to the infrared (IR) levels.

In flow conditions where the diatomic nonequilibrium is dominant, the EM coupled models of EM-atom and EM-air represent improved accuracy when used to predict the initial rising rate and the peak value of diatomic radiation and small amounts of atomic radiation in comparison with the 2T-QSS model. With regard to the 2T-QSS model, it greatly overestimates the measured peak intensity because the calculated free electron temperature is higher than those by the EM coupled models.

Under flow conditions where the atomic nonequilibrium is dominant, the spatial distributions of the intensity and electron number density are much more accurately predicted by the EM coupled models of EM-atom and EM-air than by the 2T-QSS model. Moreover, the initial intensity rises of the VUV and the near-IR range are well predicted by the EM coupled models because the atomic heavy-particle impact excitations are accurately described in the EM coupled models. The 2T-QSS model estimates the intensity increment rate reasonably but fails to determine the proper starting position of the initial intensity rise.

In all flow conditions of the high-enthalpy flows analyzed in the present study, it is observed that the EM-air model more accurately predicts measured nonequilibrium radiation in comparison with the EM-atom model. This occurs because the electronic populations of the molecules are more rigorously evaluated in the EM-air model by removing the QSS assumption of the molecular electronic states, which overestimates the state populations.

ACKNOWLEDGMENTS

The authors thank Prof. O. Zatsarinny at Drake University for providing the electron impact rate parameters for N and O. We also gratefully acknowledge Dr. B. A. Cruden at NASA Ames Research Center for providing the smearing function parameters and MATLAB files. This work was supported by the National Research Foundation of Korea (NRF) grant funded by the Korea Government (Ministry of Education) (Grant No. 2017032013).

[1] C. Park, *Nonequilibrium Hypersonic Aerothermodynamics* (John Wiley and Sons, New York, 1990).
[2] J. Grinstead, M. Wilder, J. Olejniczak, D. Bogdanoff, G. Allen, K. Dang, and M. Forrest, in *Proceedings of the 46th AIAA Aerospace Sciences Meeting and Exhibit, Reno, NV* (AIAA, Reston, VA, 2008), paper AIAA 2008-1244.
[3] B. A. Cruden and A. M. Brandis, in *Proceedings of the 47th AIAA Thermophysics Conference, Denver, CO* (AIAA, Reston, VA, 2017), paper AIAA 2017-4535.
[4] A. M. Brandis and B. A. Cruden, in *Proceedings of the 55th AIAA Aerospace Sciences Meeting, Grapevine, TX* (AIAA, Reston, VA, 2017), paper AIAA 2017-1145.
[5] A. M. Brandis and B. A. Cruden, in *Proceedings of the 2018 Joint Thermophysics and Heat Transfer Conference, Atlanta, GA* (AIAA, Reston, VA, 2018), paper AIAA 2018-3437.
[6] B. A. Cruden and A. M. Brandis, *Electric arc shock tube (EAST) test data*, https://data.nasa.gov/docs/datasets/aerothermodynamics/EAST/index.html (NASA ARC, US, 2017).
[7] C. Johnston, in *Proceedings of the 46th AIAA Aerospace Sciences Meeting and Exhibit, Reno, NV* (AIAA, Reston, VA, 2008), paper AIAA 2008-1245.
[8] D. F. Potter, Ph.D. thesis, University of Queensland, 2011.
[9] A. Lemal, C. M. Jacobs, M. Y. Perrin, C. O. Laux, P. Tran, and E. Raynaud, J. Thermophys. Heat Transf. **30**, 197 (2016).
[10] M. Panesi, Y. Babou, and O. Chazot, in *Proceedings of the 40th Thermophysics Conference, Seattle, WA* (AIAA, Reston, VA, 2008), paper AIAA 2008-3812.
[11] C. O. Johnston, B. R. Hollis, and K. Sutton, J. Spacecr. Rockets **45**, 879 (2008).
[12] A. Kramida, Y. Ralchenko, J. Reader, and N. A. Team, NIST Atomic Spectra Database, ver. 5.5.6, http://www.nist.gov/pml/data/asd.cfm [online database] (NIST, US, 2018).
[13] C. O. Laux, HTGL Report T-288 (1993).
[14] P. J. Linstrom and W. G. Mallard, NIST Chemistry Webbook, NIST Standard Reference Database Number 69, http://webbook.nist.gov (NIST, US, 1996).
[15] S. Chauveau, M.-Y. Perrin, P. Rivière, and A. Soufiani, J. Quant. Spectrosc. Radiat. Transf. **72**, 503 (2002).
[16] S. Y. Hyun, Ph.D. thesis, Korea Advanced Institute of Science and Technology, 2009.
[17] R. C. Millikan and D. R. White, J. Chem. Phys. **39**, 3209 (1963).
[18] J. G. Kim and I. D. Boyd, Chem. Phys. **415**, 237 (2013).
[19] J. G. Kim and G. Park, Phys. Fluids **30**, 016101 (2018).
[20] J. P. Appleton and K. N. C. Bray, J. Fluid Mech. **20**, 659 (1964).
[21] P. A. Gnoffo, R. N. Gupta, and J. L. Shinn, NASA TP-2867 (1989).
[22] C. Park, R. L. Jaffe, and H. Partridge, J. Thermophys. Heat Transf. **15**, 76 (2001).
[23] C. Park, in *Proceedings of the 48th AIAA Aerospace Sciences Meeting, Orlando, FL* (AIAA, Reston, VA, 2010), paper AIAA 2010-911.
[24] V. Laporta and D. Bruno, J. Chem. Phys. **138**, 104319 (2013).
[25] V. Laporta, K. L. Heritier, and M. Panesi, Chem. Phys. **472**, 44 (2016).

[26] M. Panesi, T. E. Magin, A. Bourdon, A. Bultel, and O. Chazot, J. Thermophys. Heat Transf. **25**, 361 (2011).
[27] J. G. Kim and I. D. Boyd, J. Thermophys. Heat Transf. **29**, 241 (2015).
[28] A. Bourdon and P. Vervisch, Phys. Rev. E **54**, 1888 (1996).
[29] A. Bourdon, Y. Teresiak, and P. Vervisch, Phys. Rev. E **57**, 4684 (1998).
[30] R. M. Frost, P. Awakowicz, H. P. Summers, and N. R. Badnell, J. Appl. Phys. **84**, 2989 (1998).
[31] S. S. Tayal, Astrophys. J. Suppl. Ser. **163**, 207 (2006).
[32] Y. Wang, O. Zatsarinny, and K. Bartschat, Phys. Rev. A **89**, 062714 (2014).
[33] W. M. Huo, Y. Liu, M. Panesi, A. Wray, and D. F. Carbon, in *Proceedings of the 53rd Aerospace Sciences Meeting, Kissimmee, FL* (AIAA, Reston, VA, 2015), paper AIAA 2015-1896.
[34] M. Gryziński, Phys. Rev. **115**, 374 (1959).
[35] H. W. Drawin and F. Emard, Phys. Lett. A **43**, 333 (1973).
[36] S. S. Tayal and O. Zatsarinny, Phys. Rev. A **94**, 042707 (2016).
[37] O. Zatsarinny and S. S. Tayal, Astrophys. J. Suppl. Ser. **148**, 575 (2003).
[38] C. J. Ciccarino and D. W. Savin, J. Thermophys. Heat Transf. **33**, 154 (2019).
[39] Y.-K. Kim and J.-P. Desclaux, Phys. Rev. A **66**, 012708 (2002).
[40] C. O. Johnston, B. R. Hollis, and K. Sutton, J. Spacecr. Rockets **45**, 1185 (2008).
[41] A. Bultel, B. G. Chéron, A. Bourdon, O. Motapon, and I. F. Schneider, Phys. Plasmas **13**, 043502 (2006).
[42] S. T. Surzhikov, J. Heat Transf. **134**, 031002 (2012).
[43] J. Annaloro, A. Bultel, and P. Omaly, J. Thermophys. Heat Transf. **28**, 608 (2014).
[44] C. O. Johnston and M. Panesi, Phys. Rev. Fluids **3**, 013402 (2018).
[45] D. C. Cartwright, S. Trajmar, A. Chutjian, and W. Williams, Phys. Rev. A **16**, 1041 (1977).
[46] T. Majeed and D. J. Strickland, J. Phys. Chem. Ref. Data **26**, 335 (1997).
[47] P. V. Johnson, C. P. Malone, I. Kanik, K. Tran, and M. A. Khakoo, J. Geophys. Res-Space Phys. **110**, 1 (2005).
[48] Y. Itikawa, J. Phys. Chem. Ref. Data **35**, 31 (2006).
[49] P. Teulet, J. P. Sarrette, and A. M. Gomes, J. Quant. Spectrosc. Radiat. Transf. **62**, 549 (1999).
[50] G. G. Chernyi and S. A. Losev, International Science & Technology Center Report (1999).
[51] C. Park, in *Proceedings of the 46th Aerospace Sciences Meeting and Exhibit, Reno, NV* (AIAA, Reston, VA, 2008), paper AIAA 2008-1206.
[52] A. Lemal, C. M. Jacobs, M. Y. Perrin, C. O. Laux, P. Tran, and E. Raynaud, J. Thermophys. Heat Transf. **30**, 226 (2016).
[53] C. Park, in *Proceedings of the 46th Aerospace Sciences Meeting and Exhibit, Reno, NV* (AIAA, Reston, VA, 2008), paper AIAA 2008-1446.
[54] C. O. Johnston, B. R. Hollis, and K. Sutton, J. Spacecr. Rockets **45**, 865 (2008).
[55] W. Cunto, C. Mendoza, F. Ochsenbein, and C. J. Zeippen, Astron. Astrophys. **275**, L5 (1993).
[56] G. Peach, Mon. Not. Roy. Astron. Soc. **124**, 371 (1962).
[57] J. C. Morris, R. U. Krey, and G. R. Bach, J. Quant. Spectrosc. Radiat. Transf. **6**, 727 (1966).
[58] W. H. Soon and J. A. Kunc, Phys. Rev. A **41**, 4531 (1990).
[59] S. Chauveau, C. Deron, M.-Y. Perrin, P. Rivière, and A. Soufiani, J. Quant. Spectrosc. Radiat. Transf. **77**, 113 (2003).
[60] J. J. Olivero and R. L. Longbothum, J. Quant. Spectrosc. Radiat. Transf. **17**, 233 (1977).
[61] A. Brandis, C. Johnston, M. Panesi, B. Cruden, D. Prabhu, and D. Bose, in *Proceedings of the 51st AIAA Aerospace Sciences Meeting, Grapevine, TX* (AIAA, Reston, VA, 2013), paper AIAA 2013-1055.
[62] H. Lomax, NASA TN D-4703 (1968).
[63] D. H. Crandall, W. E. Kauppila, R. A. Phaneuf, P. O. Taylor, and G. H. Dunn, Phys. Rev. A **9**, 2545 (1974).
[64] A. E. Orel, T. N. Rescigno, and B. H. Lengsfield III, Phys. Rev. A **42**, 5292 (1990).
[65] D. A. Little, K. Chakrabarti, J. Z. Mezei, I. F. Schneider, and J. Tennyson, Phys. Rev. A **90**, 052705 (2014).
[66] S. Y. Hyun, C. Park, and K.-S. Chang, J. Thermophys. Heat Transf. **23**, 641 (2009).